Available online at www.sciencedirect.com
ScienceDirect
Trans. Nonferrous Met. Soc. China 35(2025) 1729−1741

Transactions of
Nonferrous Metals
Society of China
www.tnmsc.cn

Simultaneous improvement of strength and ductility in selective laser melted low Sc content Al−Mg−Mn−Sc−Zr alloy via aging treatment

Yong-kang CHEN[1], Yao-xiang GENG[1], Xiao WANG[1], Zhi-fa SHAN[1], Zhi-jie ZHANG[1], Hong-bo JU[1,2]

1. School of Materials Science and Engineering, Jiangsu University of Science and Technology,
Zhenjiang 212003, China;
2. Department of Mechanical Engineering, CEMMPRE-Centre for Mechanical Engineering,
ARISE, CEMMPRE, University of Coimbra, Coimbra 3030-788, Portugal

Received 27 October 2023; accepted 3 June 2024

Abstract: To improve the processability and mechanical properties of the selective laser melting (SLM) low Sc content Al−Mg−Sc−Zr alloy, Mn was used to partially replace Mg. The processability, microstructure, and mechanical properties of the SLM-fabricated Al−Mg−Mn−Sc−Zr alloy were systematically investigated by density measurement, microstructure characterization, and tensile testing. The results revealed that dense samples could be obtained by adjusting the SLM process parameters. The alloy exhibited a fine equiaxed-columnar bimodal grain microstructure. The presence of primary Al_3Sc and α-Al(Mn,Fe)Si particles contributed to the grain refinement of the alloy with an average grain size of 4.63 μm. Upon aging treatment at 350 °C for 2 h, the strength and elongation of the alloy were simultaneously improved due to the precipitation of Al_3Sc nanoparticles and the formation of the 9R phase. This study demonstrates that the strength−plasticity trade-off of the aluminum alloy can be overcome by utilizing SLM technology and subsequent post-heat treatment to induce the formation of the long-period stacked ordered phase.

Key words: selective laser melting; low Sc content Al−Mg−Mn−Sc−Zr alloy; 9R phase; Al_3Sc nanoparticle; strength−plasticity trade-off

---

1 Introduction

Selective laser melting (SLM) is an essential additive manufacturing (AM) technology that enables the efficient manufacture of complex structural metal components [1−3]. Aluminum alloys, are renowned for their exceptional properties, such as high specific strength, excellent thermal and electrical conductivity, and superior corrosion resistance, showing extensive applications in aerospace, automotive, and other industries [4,5].

The alloying with high contents of Sc and Zr elements can effectively enhance the SLM processability and mechanical properties of Al−Mg (5xxx) and Al−Mn (3xxx) series aluminum alloys [6]. Scalmalloy® (Al−4.6Mg−0.66Sc−0.42Zr) alloy was first designed for SLM [7]. The alloy exhibited outstanding mechanical properties with yield strength (YS) and ultimate tensile strength (UTS) over 520 MPa. The high strength of the Scalmalloy® alloy primarily originated from the combined effects of grain refinement strengthening caused by the primary $Al_3(Sc,Zr)$ particles, solid solution strengthening induced by Mg, and precipitation strengthening resulting from the secondary Al_3Sc nanoparticles [8]. JIA et al [9] suggested that substituting Mn for Mg in 5xxx series aluminum alloys can enhance the mechanical properties of the alloy effectively. Furthermore, the UTS of the SLM-fabricated Al−Mn−Mg−Sc−Zr alloy could be further improved to over 700 MPa by

---

Corresponding author: Yao-xiang GENG, Tel: +86-13952871355, E-mail: yaoxianggeng@163.com

https://doi.org/10.1016/S1003-6326(25)66779-3

1003-6326/© 2025 The Nonferrous Metals Society of China. Published by Elsevier Ltd & Science Press
This is an open access article under the CC BY-NC-ND license (http://creativecommons.org/licenses/by-nc-nd/4.0/)

increasing the content of Mg+Mn and/or Sc+Zr elements [10−12]. However, the high content of Sc element (>0.5 wt.%) in these high-performance Al−Mn/Al−Mg-based aluminum alloys poses a challenge for practical applications. The Sc-containing Al−Mg-based aluminum alloys currently used in the industry usually have a low Sc content (<0.4 wt.%) [13], but the low nucleation concentration leads to poor processability during SLM of those alloys [14].

Overcoming the strength−ductility trade-off is a critical goal in alloy design. One possible solution is to incorporate twins and/or the long-period stacking ordered (LPSO) phase in the alloys. The twins and the LPSO phase serve as effective barriers, impeding the motion of dislocations within grains, thereby enhancing both the strength and strain-hardening ability of metallic materials. The 9R phase is commonly formed through the dissociation of $\Sigma3\{112\}$ incoherent twin boundaries (ITBs) in FCC crystals [15]. Twins and the LPSO phase are commonly observed in metals with low stacking fault energy (SFE), such as stainless steel (10−20 mJ/m^2), Cu (~45 mJ/m^2), and Ag (~16 mJ/m^2) [16−19]. In contrast, the formation of twins and LPSO phase in bulk aluminum alloys is challenging due to their high SFE (120−166 mJ/m^2) [20−22]. Recently, LI et al [23] have discovered twins and 9R-LPSO phase in the SLM-fabricated high Sc content Al−Mg−Si−Sc−Zr alloy. The presence of the 9R phase resulted in a significant improvement in the mechanical properties of the alloy. However, twins and LPSO phase were not observed in the low Sc content Al−Mg−Sc−Zr aluminum alloys.

In this study, to improve the processability and mechanical properties of the SLM-fabricated low-Sc content Al−Mg−Sc−Zr aluminum alloy, Mn was chosen to partially substitute the Mg element. By adjusting the SLM process parameters, the dense Al−Mg−Mn−Sc−Zr samples were fabricated. The subsequent aging treatment resulted in the precipitation of Al_3Sc nanoparticles and the 9R phase, which simultaneously improved the strength and plasticity of the alloy.

2 Experimental

2.1 Preparation of alloy powder

A pre-alloyed Al−2.66Mg−2.01Mn−0.37Sc−0.33Zr−0.18Fe−0.10Si (wt.%) powder was prepared using the vacuum induction gas atomization (VIGA) method. The chemical compositions of the powder were determined using the inductively coupled plasma atomic emission spectroscopy (ICP-AES).

2.2 SLM process

The specimens with dimensions of 50 mm (length) × 15 mm (width) × 15 mm (height) were fabricated using an EP M250 machine. The process parameters are listed in Table 1. After printing, the specimens were aged at 350 and 400 °C for 2, 4, 6, 8, 10, 12, 18, 24, and 48 h, respectively.

Table 1 SLM process parameters

Parameter	Value
Laser power/W	250, 350
Laser beam diameter/μm	100
Powder layer thickness/μm	30
Hatch spacing/μm	100
Laser scanning speed/(mm·s^{-1})	800, 900, 1000, 1100, 1200
Angle of rotation/(°)	67

2.3 Microstructure and phase characterization

The microstructural analysis of the SLM-fabricated specimens was conducted by scanning electron microscopy (SEM, SM−6480) and transmission electron microscopy (TEM, JEM−2010F), respectively. An energy dispersive X-ray spectroscopy (EDX) was used to analyze the components of the specimens. The crystallographic orientation and grain size of the specimens were examined by the electron backscattered diffraction (EBSD, OXFORD Nordlys Nano). A Bruker D8 Focus X-ray diffractometer (Cu K_α, 0.15406 nm) was used for phase identification of the specimens.

2.4 Property tests

The mass density of the specimens was determined using the Archimedes method. The tensile properties of the alloy were evaluated using a UTM5105 universal testing machine at a constant strain rate of 1 mm/min following the ASTM E8-04 standard. The data were averaged from three specimens. The microstructure and mechanical properties of the specimens were tested on the specimens fabricated at a laser scanning speed of 800 mm/s and a laser power of 350 W.

3 Results

3.1 Processability

Figure 1 illustrates the SEM microstructures of the Al−Mg−Mn−Sc−Zr alloys fabricated at different process parameters. At a laser power of 250 W, the alloys exhibited numerous keyholes and cracks. Notably, the keyholes were mainly penetrated by cracks (Figs. 1(a−c)). Conversely, for the alloys fabricated at a laser power of 350 W and scanning speeds between 800 and 1000 mm/s, only a few metallurgical holes were observed (Figs. 1(d) and (e)). However, keyholes and cracks appeared when the laser scanning speeds increased to 1200 mm/s (Fig. 1(f)).

Relative density is a crucial indicator to assess the processability of the SLM-fabricated alloy [24]. The relative densities of the alloys exhibited a declining trend as the laser scanning speed increased (Fig. 2). At a laser power of 350 W, the alloys fabricated at scanning speeds ranging from 800 to 1000 mm/s consistently achieved relative densities exceeding 99.5%, showing excellent processability. However, when the laser scanning speed was further increased to 1100 mm/s, the relative density of the alloy rapidly dropped to (97.93±0.06)% due to the presence of keyholes and cracks. At 250 W, the relative densities for all alloys remained below 98%.

3.2 Microstructure

3.2.1 As-built alloy

The as-built alloy displayed a bimodal grain structure. The equiaxed grains were about 1 μm, while columnar grains varied in width from several

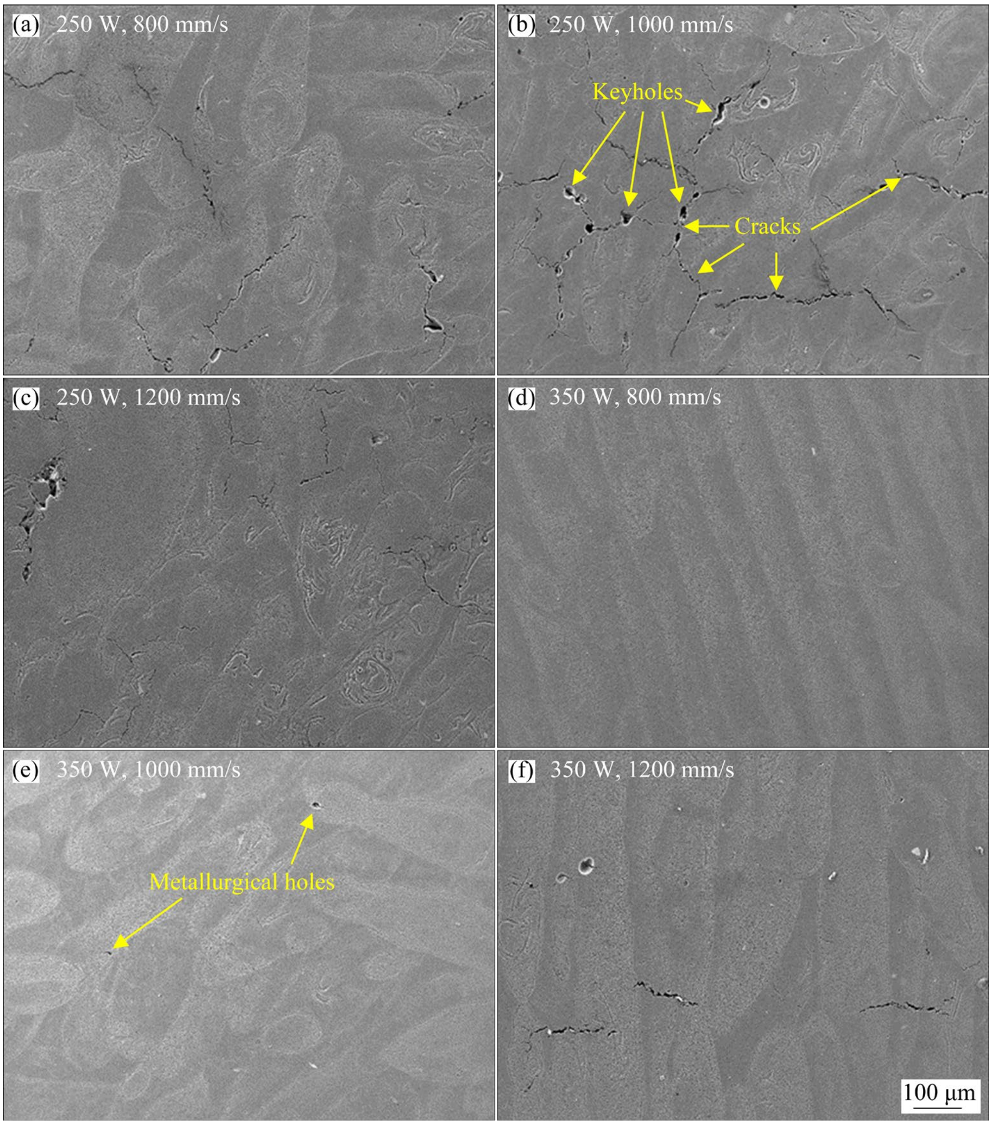

Fig. 1 SEM images of alloy fabricated at different laser powers and laser scanning speeds

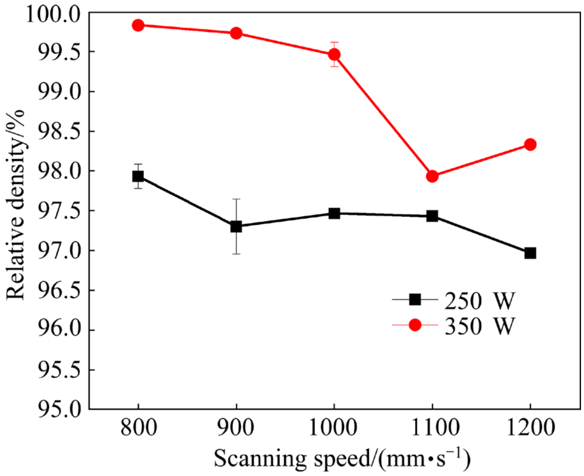

Fig. 2 Relative densities of alloys fabricated at different process parameters

microns to tens of microns, with lengths in the tens of microns (Figs. 3(a) and (b)). The average grain size of the alloy was about 4.63 μm (Fig. 3(d)). Besides, the alloy exhibited a weak ⟨001⟩ texture, with minimum and maximum texture densities of 0.55 and 1.49, respectively (Fig. 3(c)).

Figure 4 exhibits the high-angle annular dark field (HAADF) TEM images and corresponding EDX mappings obtained from the equiaxed and columnar grain regions, respectively. The precipitates with sizes ranging from tens to hundreds of nanometers were observed in both the α-Al grains and grain boundaries (Figs. 4(a) and (c)). The EDX analysis confirmed the segregation of Mg, Si, Mn, Fe, O, and Sc elements (Figs. 4(b) and (d)). Further TEM analysis indicated the presence of $Al_6(Mn,Fe)$ and α-Al(Mn,Fe)Si phases in the grains (Figs. 5 and 6). The orientation relationship between α-Al(Mn,Fe)Si and α-Al matrix was determined to be $[532]_{\alpha\text{-Al(Mn,Fe)Si}}//[001]_{\alpha\text{-Al}}$ with a semi-coherent interface (Fig. 6). The EDX results also suggested the possible presence of Mg_2Si, Al_3Sc, and oxide phases [25−27]. The regions surrounding the precipitates in equiaxed and columnar grains exhibited a uniform face-centered cubic (FCC) structure (Fig. 7).

3.2.2 Aged alloy

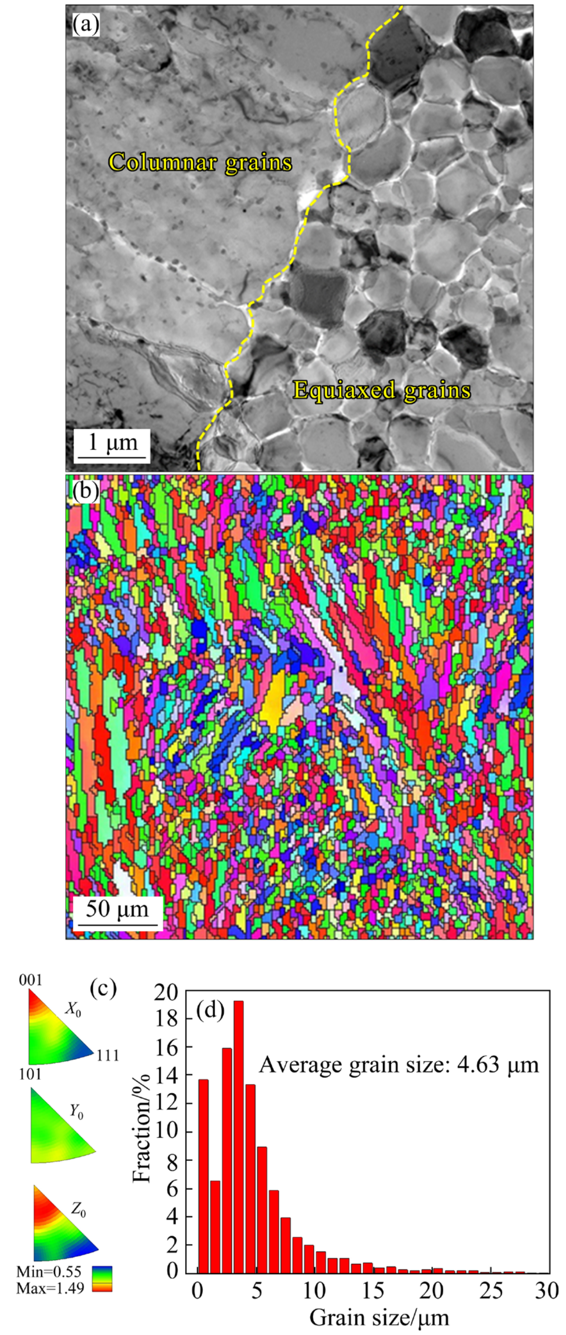

Fig. 3 TEM bright field image (a), EBSD map (b), pole figures (c), and grain size distribution (d) of alloy

Aging treatment is known to be an effective way to improve the strength of Sc- and Zr-containing aluminum alloys [28]. Figure 8 presents TEM images of the alloy after being aged at 350 °C for 2 h. The SAED patterns obtained from the α-Al matrix indicated the precipitation of Al_3Sc nanoparticles in both equiaxed and columnar grains, as depicted in the insets in Figs. 8(a) and (b), respectively. In addition, high-resolution TEM images revealed blocky precipitates with dimensions in the tens of nanometers in the grains (Fig. 8(c)). The corresponding FFT and inverse FFT images demonstrated that these precipitates were the deformed 9R-LPSO phase (Figs. 8(c) and (d)). Twins and stacking faults (SFs) were observed in the 9R phase.

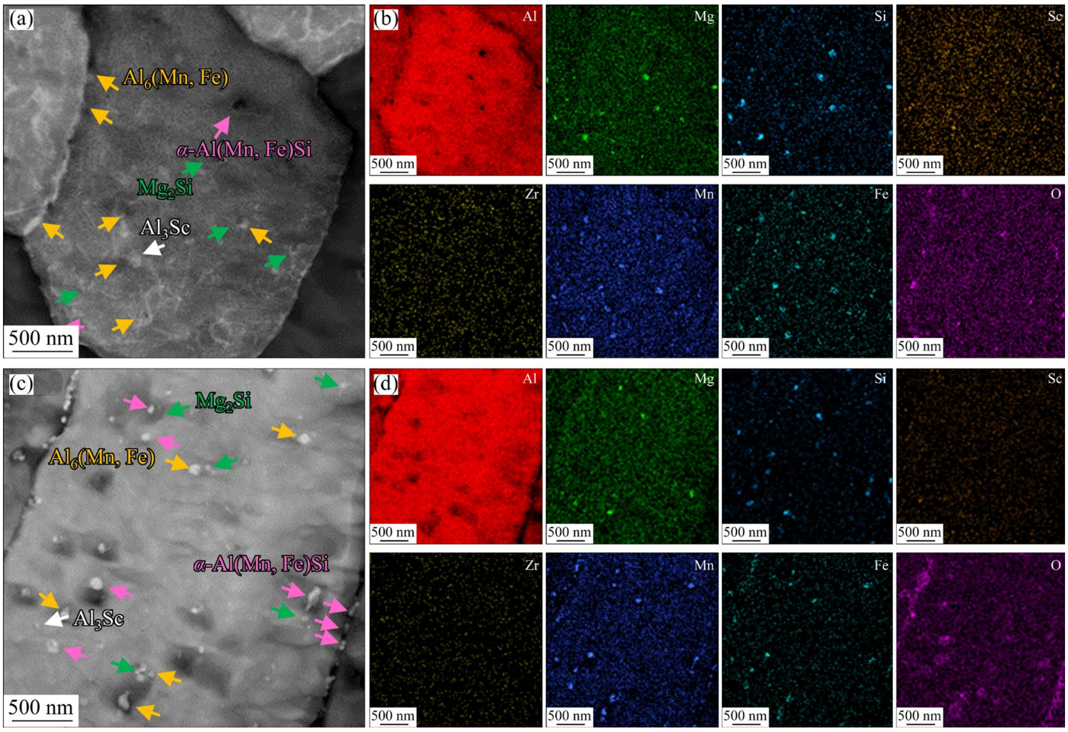

Fig. 4 HAADF TEM images (a, c) and corresponding EDX mappings (b, d) obtained from equiaxed (a, b) and columnar (c, d) grains of alloy

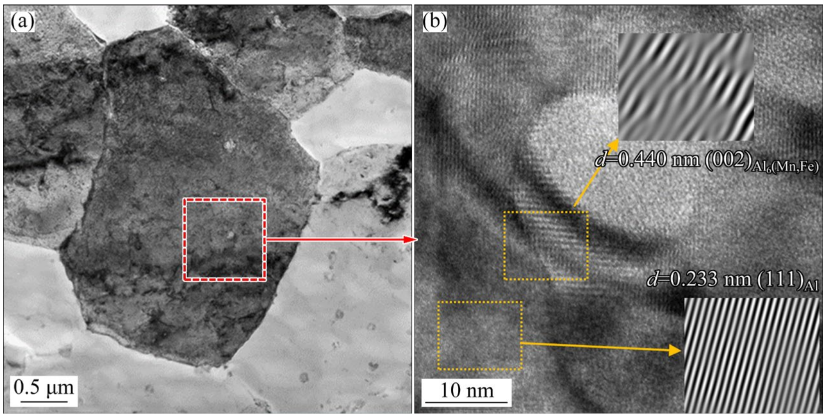

Fig. 5 TEM bright field image (a) and corresponding high-resolution TEM image (b) of alloy

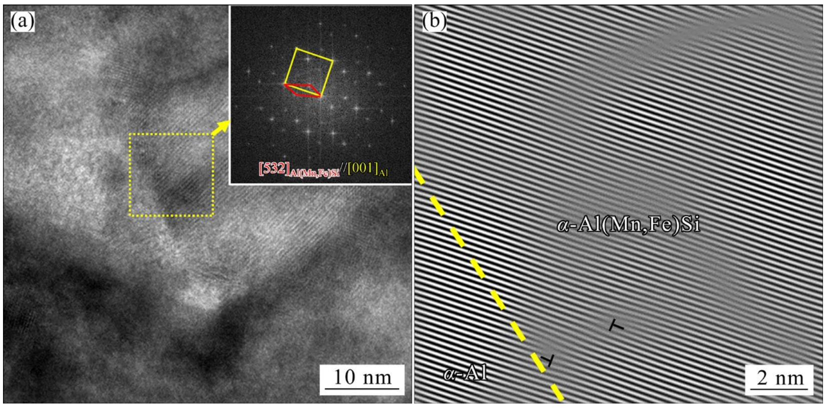

Fig. 6 High-resolution TEM image (a), and inverse fast Fourier transformed (FFT) image (b) obtained from FFT image inserted in (a)

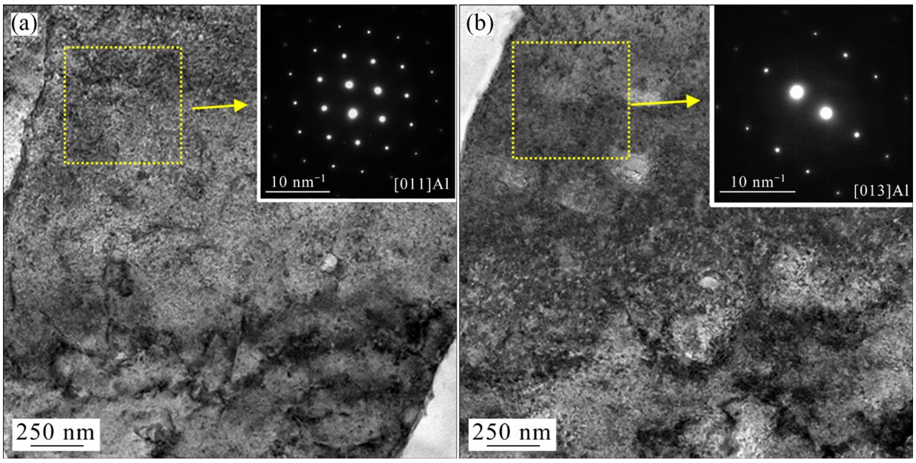

Fig. 7 TEM bright field images and corresponding SAED patterns (insets) obtained from outside of precipitates in equiaxed (a) and columnar (b) grains of alloy

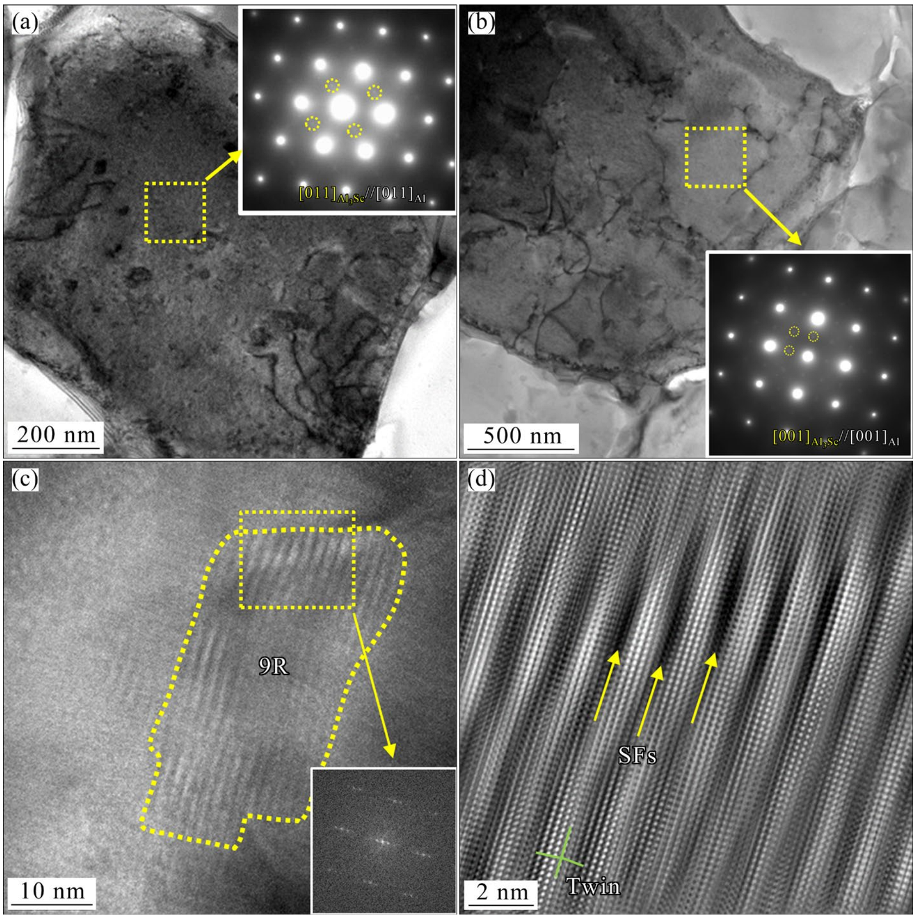

Fig. 8 TEM bright field images (a, b) and corresponding SAED patterns (insets) obtained from equiaxed (a) and columnar (b) grains, high-resolution TEM and FFT images (inset) (c), and inverse FFT image (d) of alloy after aging at 350 °C for 2 h

After aging the alloy at 350 °C for 8 h, the primary precipitates were coarse (Figs. 9(a) and (c)). Besides, a significant number of secondary needle-shaped particles precipitated within the columnar grains. EDX analysis confirmed that these particles could be identified as the $Al_6(Mn,Fe)$ phase (Figs. 9(b) and (d)). Furthermore, the high-resolution TEM images and inverse FFT patterns determined that a small number of the residual 9R phases with dimensions less than 10 nm remained in the alloy (Fig. 10). Figure 11 displays the XRD patterns of the Al−Mg−Mn−Sc−Zr alloy. For the as-built and aged (350 °C, 2 h) alloys, only the α-Al phase was observed in the XRD patterns. However, when the aging time was increased to 8 h, the $Al_6(Mn,Fe)$ phase appeared.

3.3 Mechanical properties

Figure 12(a) depicts the engineering stress−strain curves of the as-built and 350 °C-aged alloys for various time. The values of YS, UTS, and elongation are summarized in Fig. 12(b). For the as-built alloy, the YS, UTS, and elongation values were measured to be (220.5±11.6) MPa, (266.1±14.8) MPa, and (10.8±2.0)%, respectively. After aging the alloy at 350 °C for 2 h, both the strength and elongation of the alloy were improved synchronously, with a YS of (318.0±8.1) MPa, an UTS of (390.0±21.9) MPa, and an elongation of (14.8±2.4)%. Upon extending the aging time to 8 h,

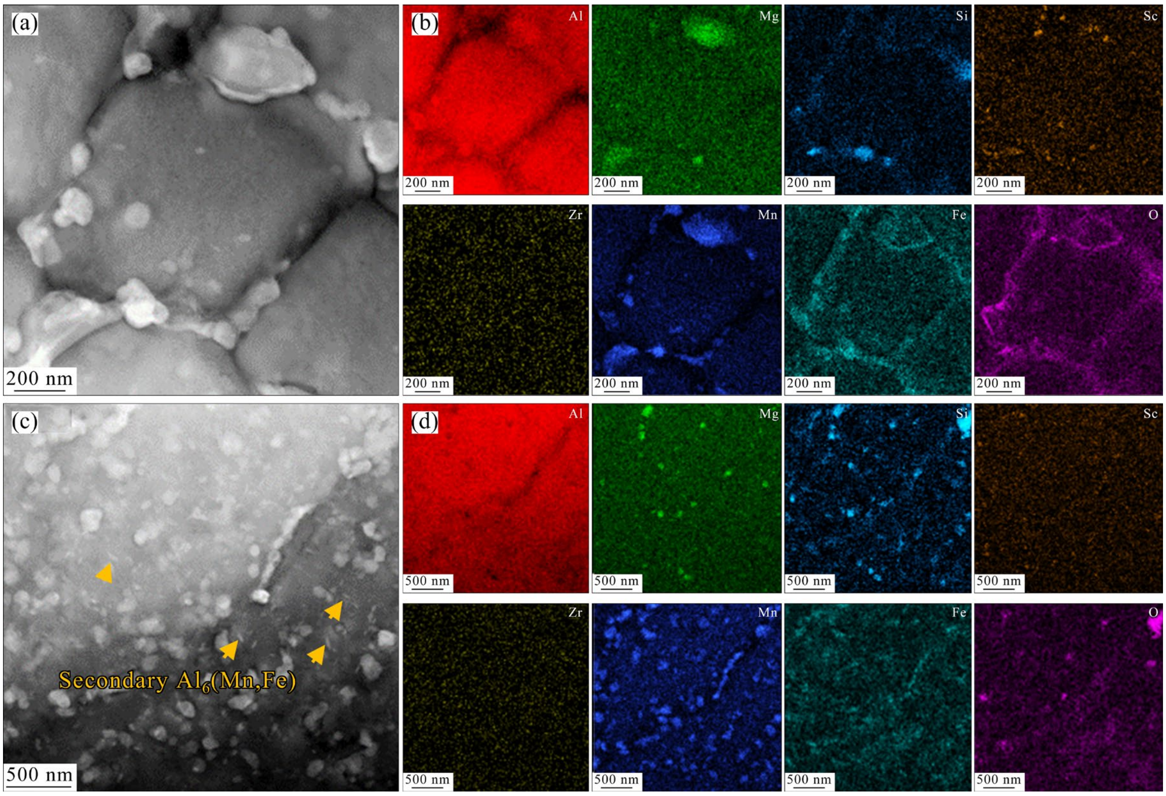

Fig. 9 HAADF TEM images (a, c) and corresponding EDX mappings (b, d) obtained from equiaxed (a, b) and columnar (c, d) grain regions of alloy after aging at 350 °C for 8 h

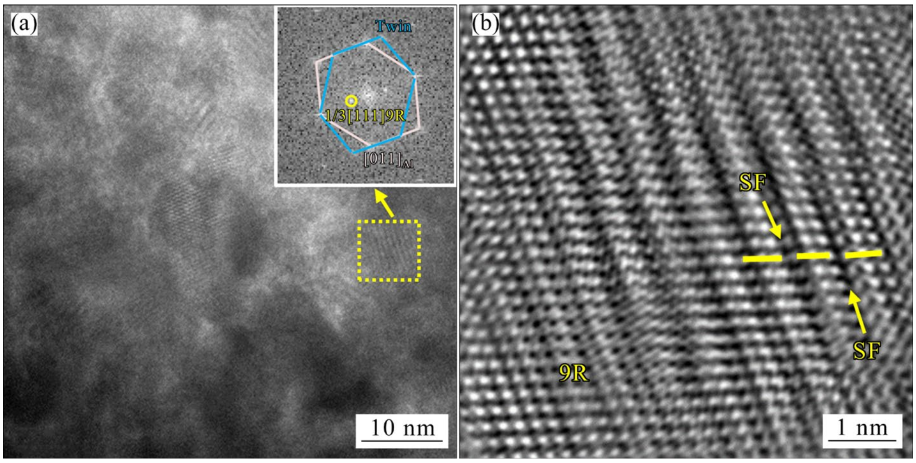

Fig. 10 High-resolution TEM image (a) and FFT pattern (inset) of alloy after aging at 350 °C for 8 h (FFT pattern indicates typical twin structures in [111] texture and 9R superlattice spots), and inverse FFT pattern showing presence of SFs on every third close-packed plane (b)

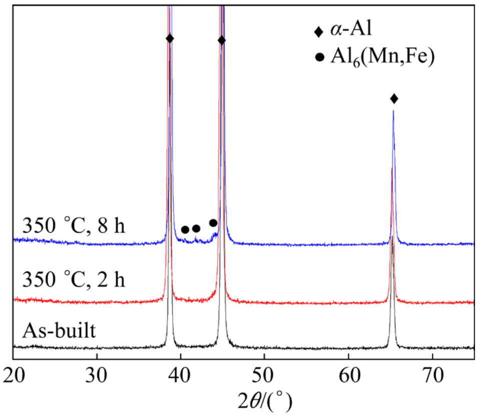

Fig. 11 XRD patterns of as-built and 350 °C-aged alloys

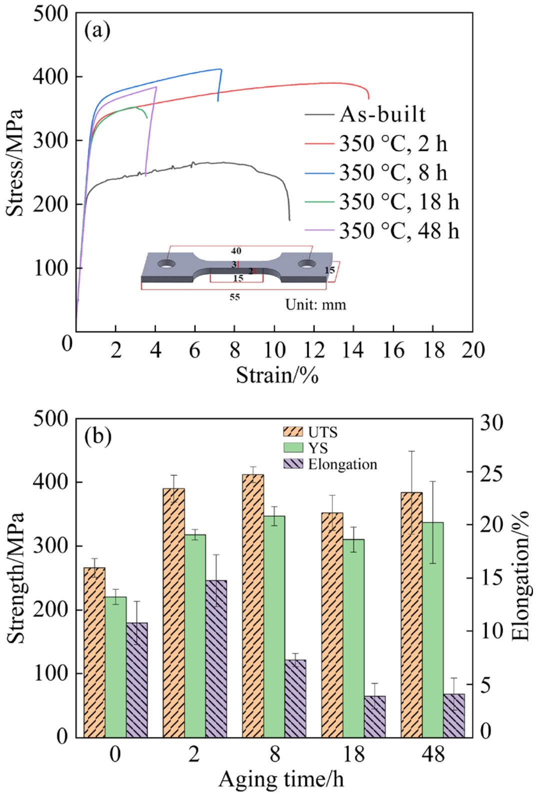

Fig. 12 Stress−strain curves (a) and mechanical properties (b) of as-built and 350 °C-aged alloys

the YS and UTS of the alloy further increased to (347.0±15.0) MPa and (411.9±12.5) MPa, respectively; however, the elongation decreased to (7.3±0.6)%. Subsequently, with an increase in aging time to 18 h, both the strength and elongation of the alloy concurrently decreased.

4 Discussion

4.1 Processability

The morphology of the upper surface of SLM-fabricated alloys is influenced by various factors such as the melting degree, dynamics of the melt pool, and solidification properties. These factors, in turn, affect the formation of defects in the SLM-fabricated alloy [29]. A comprehensive description of these factors can be achieved by considering the volumetric energy density (ED_v) [30]. The ED_v is calculated as $ED_v=P/(vht)$, where P is the laser power, v is the scanning speed, h is the hatch spacing, and t is the layer thickness. Based on this formula, the ED_v values for the alloys fabricated under different process conditions were calculated, and the results are listed in Table 2.

Table 2 ED_v values of alloy fabricated at different process parameters

Laser power/W	ED_v/(J·mm^{-3})				
	800 mm/s	900 mm/s	1000 mm/s	1100 mm/s	1200 mm/s
250	104.1	92.6	83.3	75.8	69.4
350	145.8	129.6	116.7	106.1	97.2

Figure 13 presents the SEM images of the upper surface of the SLM-fabricated Al−Mg−Mn−Sc−Zr alloys. At a laser power of 250 W, numerous spheres were observed on the top surface of the alloy (Figs. 13(a−c)). At a laser power of 350 W and a laser scanning speed ranging from 800 to 1000 mm/s, only a few splashes were observed on the upper surface of the alloys (Figs. 13(d) and (e)). However, when the laser scanning speed was increased to 1200 mm/s, the balling phenomenon began to appear on the upper surface of the alloy (Fig. 13(f)).

In the SLM-fabricated alloy, the small splashes may have less impact on the processability [31,32]. At a laser power of 350 W and a laser scanning speed of 800−1000 mm/s, the high ED_v (116.7−145.8 J/mm^3) results in a higher energy input, which increases the temperature of the molten pool. Consequently, the surface tension and viscosity of the molten material decrease, allowing the molten material to spread and flow more smoothly throughout the pool. As a result, the molten material becomes more resistant to the fragmentation [33]. Consequently, a continuous and uniform laser scanning path is achieved, which can effectively prevent the formation of balls (Figs. 13(d) and (e)). This reduces the likelihood of defects during the remelting process, thereby enhancing processability

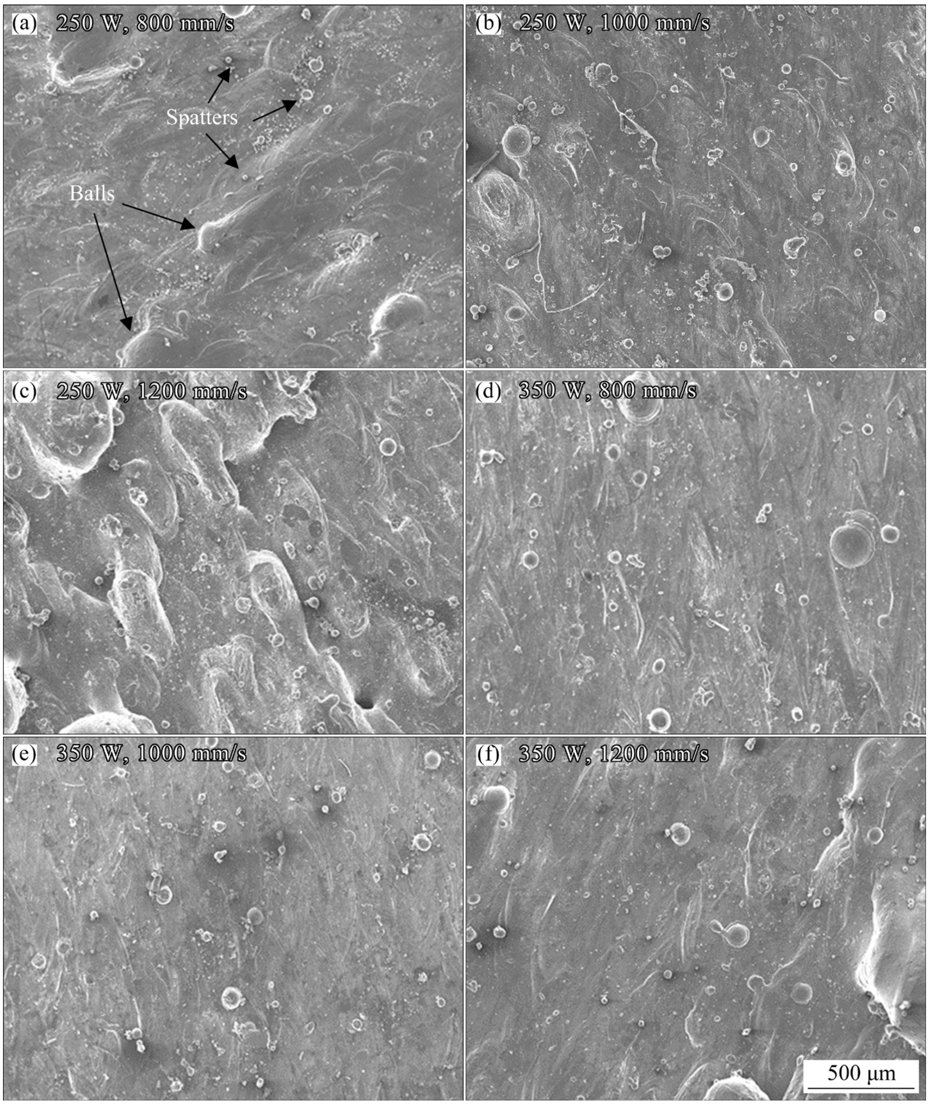

Fig. 13 SEM images of upper surface of alloy fabricated at different process parameters

of the alloy (Fig. 1). On the contrary, insufficient laser energy input leads to the intermittent spread of the molten pool during SLM processes, causing the balling phenomenon. These residual molten balls might not fully liquefy during the re-melting process for subsequent layers, hindering the uniform deposition of powder layers and inadequate gap filling on irregular surfaces [34], and thus resulting in the formation of keyholes within the alloy (Figs. 1 and 2). Furthermore, the SLM-fabricated alloys often experience elevated levels of thermally induced residual stresses due to the rapid cooling inherent in the SLM process, which tend to concentrate in irregular defect regions such as keyholes. If these residual stresses exceed the YS of the alloys during cooling, cracks may form [35,36].

4.2 Microstructure

In commercial Al−Mn-based alloys, impurities like Fe and Si commonly appear and combine with Al and Mn to form cubic α-Al(Mn,Fe)Si and orthorhombic Al_6(Mn,Fe) phases [37]. In alloys with high Si content, the α-Al(Mn,Fe)Si phase remains stable, preventing the formation of Al_6(Mn,Fe) phases. Conversely, in alloys with low Si levels, the α-Al(Mn,Fe)Si phase forms during initial heating at lower temperatures but dissipates at higher temperatures, ultimately resulting in the precipitation of the more stable Al_6(Mn,Fe) phase [25,38].

In our study, both α-Al(Mn,Fe)Si and Al_6(Mn,Fe) phases were observed through TEM analysis (Figs. 5 and 6), which can be attributed to the low Si content in the alloy. Besides, the presence of Mg and Sc elements in the alloy promotes the formation of the Mg_2Si and Al_3Sc phases (Figs. 4 and 7). In SLM-fabricated Sc-containing aluminum alloys, the primary Al_3Sc nanoparticles have been found to play a crucial role in grain refinement due to their coherence with the Al matrix [39]. Recently, LI et al [25] have investigated the habit planes of dispersoids for α-Al(Mn,Fe)Si in as-cast AA3003 alloy. The results revealed that α-Al(Mn,Fe)Si dispersoids exhibit partial coherency with the Al matrix. Our research also agrees with their results (Fig. 6). The precipitation of the α-Al(Mn,Fe)Si phase may also contribute to the grain refinement in SLM-fabricated Al−Mg−Mn−Sc−Zr alloy. The combined grain refinement effect of Al_3Sc and α-Al(Mn,Fe)Si led to a smaller average grain size and a higher proportion of equiaxed grains in the current alloy compared to other Al−Mg-based aluminum alloys fabricated by SLM with similar Sc content [40]. Furthermore, the precipitation of numerous nano-particles within the grains and at the grain boundaries also hinders the growth-preferred orientations of the columnar grains (Fig. 4).

Previous studies [22,40−44] showed that adding low SFE alloying elements, such as Mg, Sc, Zr, Fe, and Si, to pure aluminum can effectively reduce the SFE of the material. However, conventional processing methods still face significant challenges in achieving twins and the LPSO phases in aluminum alloys, mainly due to the low equilibrium solid solubility of these low SFE alloying elements. During the SLM process, the melt cools rapidly at a rate of 10^5-10^6 K/s, which makes the alloy achieve supersaturated solid solutions that exceed the solid solution limits of alloying elements [45]. The unique characteristic of the SLM process promotes the formation of twins and the LPSO phase in bulk aluminum alloys.

According to EDX point measurement, the solid solution contents of Mg, Mn, Sc, Zr, Fe, and Si in α-Al of the as-built alloy were found to be 1.63 wt.%, 1.55 wt.%, 0.25 wt.%, 0.34 wt.%, 0.15 wt.%, and 0.08 wt.%, respectively. It is worth noting that the Mg and Zr elements are difficult to precipitate from α-Al, while the Sc element primarily forms Al_3Sc nanoparticles during the aging treatment at 350 °C [8,23] considering that twins and the 9R phase serve as transition structures during phase transformation [46]. Therefore, the solid solution of Fe and Si elements in the present SLM-fabricated Al−Mg−Mn−Sc−Zr alloy may significantly influence the formation of twins and the 9R phase. It is assumed that a portion of Fe and Si elements form α-Al(Mn,Fe)Si, Al_6(Mn,Fe), and Mg_2Si phases in the as-built alloy. The remaining Fe and Si elements may segregate and form clusters with Al and Mn elements. Following a 350 °C aging treatment, the strain energy between clusters and the α-Al matrix decreases, which leads to the twins precipitating from Mn, Fe, and Si-enriched areas through atom rearrangement and lattice distortions. As the aging time increases, part of the twins transform into the 9R phase through the dissociation of $\Sigma3\{112\}$ ITBs. As the aging time further increases, twins and the 9R phase transform into α-Al(Mn,Fe)Si phase, eventually decomposing into a stable Al_6(Mn,Fe) phase.

4.3 Mechanical properties

For the as-built Al−Mg−Mn−Sc−Zr alloy, several strengthening mechanisms contribute to its strength. Firstly, solid solutions of Mg, Mn, Sc, Zr, Fe, and Si elements cause atomic lattice distortion, hindering dislocation movement and increasing the strength of the alloy [47]. Secondly, the presence of Al_6(Mn,Fe), Mg_2Si, Al_3Sc, α-Al(Mn,Fe)Si, and oxide secondary phases creates obstacles to the dislocation movement, further enhancing the strength [48]. Finally, the precipitation of primary Al_3Sc and α-Al(Mn,Fe)Si has a strong grain refinement effect, as the high-density grain boundaries effectively hinder dislocation movement, leading to increased strength [49].

After an aging treatment at 350 °C for 2 h, a large amount of secondary Al_3Sc nanoparticles and the 9R phase begin to precipitate from α-Al of the alloy. The Al_3Sc nanoparticles act as strengthening agents, hindering dislocation movement and impeding grain boundary motion, thus enhancing the strength of the alloy. Moreover, the 9R phase also serves as an obstacle, storing dislocations inside grains and concurrently increasing strength and strain hardening ability in metallic materials [15]. Therefore, the increase in elongation observed in the SLM-fabricated Al−Mg−Mn−Sc−Zr alloy after aging treatment can be mainly attributed to the precipitation of the 9R phase. As the aging temperature extends to 8 h, the alloy strength is further reinforced owing to the substantial precipitation of *α*-Al(Mn,Fe)Si and/or Al_6(Mn,Fe) phases. However, with a reduction in the number and size of the 9R phase, there is a noticeable decrease in the plasticity of the material. As the aging time extends to 18 h, both the strength and ductility of the alloy decrease due to the coarsening of precipitates.

5 Conclusions

(1) The volumetric energy density ED_v greatly influenced the processability of the SLM-fabricated Al−Mg−Mn−Sc−Zr alloy. High ED_v resulted in increased energy input, which promoted the uniform spreading of the melt and produced a smooth upper surface of the alloy. This prevented the formation of keyholes and microcracks, resulting in improved densification.

(2) The alloy exhibited a microstructure with equiaxed and columnar grain regions. Various nanoparticles, including Al_6(Mn,Fe), Mg_2Si, Al_3Sc, *α*-Al(Mn,Fe)Si, and oxide phases, were observed within the alloy. The YS, UTS, and elongation values for the as-built alloy were (220.5±11.6) MPa, (266.1±14.8) MPa, and (10.8±2.0)%, respectively. After aging the alloy at 350 °C for 2 h, the Al_3Sc nanoparticles and the 9R phase were precipitated from the *α*-Al matrix, which simultaneously improved the strength and plasticity of the alloy, leading to the increased YS, UTS, and elongation values of (318.0±8.1) MPa, (390.0±21.9) MPa, and (14.8±2.4)%, respectively. However, with prolonging aging time, the 9R phase gradually transformed into a stable phase, resulting in a significant reduction in the alloy plasticity.

(3) Leveraging the inherent technical characteristics of rapid cooling in SLM, it has become feasible to create bulk aluminum alloys with LPSO phase through high concentration low SFE element alloying. This methodology proves to be highly effective in improving the mechanical properties of the alloy, making it an important advancement in the development of high-performance aluminum alloys.

CRediT authorship contribution statement

Yong-kang CHEN: Methodology, Data curation, Writing − Review & editing; **Yao-xiang GENG:** Methodology, Validation, Formal analysis, Investigation, Data curation, Writing − Original draft, Review & editing; **Xiao WANG**, **Zhi-fa SHAN**, **Zhi-jie ZHANG** and **Hong-bo JU:** Data curation.

Declaration of competing interest

The authors declare that they have no known competing financial interests or personal relationships that could have appeared to influence the work reported in this paper.

Acknowledgments

This work was supported by the National Natural Science Foundation of China (Nos. 51801079, 52001140), the National Funds Through FCT of Portugal–Fundação para a Ciência e a Tecnologia, under a scientific contract of 2021.04115.CEECIND, and the Projects of UIDB/00285/2020, and LA/0112/2020.

References

[1] IVANOVA O S, WILLIAMS C B, CAMPBELL T A. Additive manufacturing (AM) and nanotechnology: Promises and challenges [J]. Rapid Prototyping Journal, 2013, 19(5): 353−364.

[2] SUN Jian-feng, YANG Yong-qiang, WANG Di. Parametric optimization of selective laser melting for forming Ti_6Al_4V samples by Taguchi method [J]. Optics and Laser Technology, 2013, 49: 118−124.

[3] EMMELMANN C, SANDER P, KRANZ J, WYCISK E M. Laser additive manufacturing and bionics: Redefining lightweight design [J]. Physics Procedia, 2011, 12: 364−368.

[4] IMMARIGEON J P, HOLT R T, KOUL A K, ZHAO L, WALLACE W, BEDDOES J C. Lightweight materials for aircraft applications [J]. Materials Characterization, 1995, 35(1): 41−67.

[5] WANG Pei, ECKERT J, PRASHANTH K G, WU Ming-wei, KABAN I, XI Li-xia, SCUDINO S. A review of particulate-reinforced aluminum matrix composites fabricated by selective laser melting [J]. Transactions of Nonferrous Metals Society of China, 2020, 30(8): 2001−2034.

[6] LAI Yi, DENG Ying, ZHU Xin-wen, GUO Yi-fan, XU Guo-fu, HUANG Ji-wu, YIN Zhi-min. Tensile property and microstructure of Al−4.77Mn−1.37Mg−0.67Sc−0.25Zr alloy under different selective laser melting processing parameters [J]. Transactions of Nonferrous Metals Society of China, 2023, 33(2): 357−370.

[7] SCHMIDTKE K, PALM F, HAWKINS A P, EMMELMANN C. Process and mechanical properties: Applicability of a scandium modified Al-alloy for laser additive manufacturing [J]. Physics Procedia, 2011, 12: 369−374.

[8] SPIERINGS A B, DAWSON K, UGGOWITZER P J, WEGENER K. Influence of SLM scan-speed on microstructure, precipitation of Al_3Sc particles and mechanical properties in Sc- and Zr-modified Al−Mg alloys [J]. Materials & Design, 2018, 140: 134−143.

[9] JIA Qing-bo, ROMETSCH P, KÜRNSTEINER P, CHAO Qi, HUANG Ai-jun, WEYLAND M, BOURGEOIS L, WU Xin-hua. Selective laser melting of a high strength Al−Mn−Sc alloy: Alloy design and strengthening mechanisms [J].

Acta Materialia, 2019, 171: 108−118.

[10] TANG Hao, GENG Yao-xiang, BIAN Shu-nuo, XU Jun-hua, ZHANG Zhi-jie. An ultra-high strength over 700 MPa in Al−Mn−Mg−Sc−Zr alloy fabricated by selective laser melting [J]. Acta Metallurgica Sinica (English Letters), 2022, 35(3): 466−474.

[11] GENG Yao-xiang, TANG Hao, XU Jun-hua, ZHANG Zhi-jie, XIAO Ya-kai, WU Yi. Strengthening mechanisms of high-performance Al−Mn−Mg−Sc−Zr alloy fabricated by selective laser melting [J]. Science China: Materials, 2021, 64(12): 3131−3137.

[12] TANG Hao, GENG Yao-xiang, LUO Jin-jie, XU Jun-hua, JU Hong-bo, YU Li-hua. Mechanical properties of high Mg-content Al−Mg−Sc−Zr alloy fabricated by selective laser melting [J]. Metals and Materials International, 2021, 27(8): 2592−2599.

[13] ZHANG Hong-min, JIANG Peng, PAN Hai-Jun, PENG Jian, WANG Zhi-zhi, YAN Ke-tao, ZHA Min. Dynamic recrystallization-dependent high-temperature tensile properties and deformation mechanisms in Al−Mg−Sc−Zr alloys [J]. Materials Science and Engineering: A, 2023, 880: 145304.

[14] LI Rui-di, WANG Min-bo, YUAN Tie-chui, SONG Bo, CHEN Chao, ZHOU Ke-chao, CAO Peng. Selective laser melting of a novel Sc and Zr modified Al−6.2Mg alloy: Processing, microstructure, and properties [J]. Powder Technology, 2017, 319: 117−128.

[15] ZHANG Jing-fan, ZHOU Deng-shan, PANG Xue-yong, ZHANG Bo-wen, LI Yue, SUN Bin-han, VALIEV R Z, ZHANG De-liang. Deformation-induced concurrent formation of 9R phase and twins in a nanograined aluminum alloy [J]. Acta Materialia, 2023, 244: 118540.

[16] LU Lei, SHEN Yong-feng, CHEN Xian-hua, QIAN Li-hua, LU Ke. Ultrahigh strength and high electrical conductivity in copper [J]. Science, 2004, 304(5669): 422−426.

[17] ZHANG X, WANG H, CHEN X H, LU L, LU K, HOAGLAND R G, MISRA A. High-strength sputter-deposited Cu foils with preferred orientation of nanoscale growth twins [J]. Applied Physics Letters, 2006, 88(17): 173116.

[18] BUFFORD D, WANG H, ZHANG X. High strength, epitaxial nanotwinned Ag films [J]. Acta Materialia, 2011, 59(1): 93−101.

[19] WANG Y M, SANSOZ F, LAGRANGE T, OTT R T, MARIAN J, BARBEE T W Jr, HAMZA A V. Defective twin boundaries in nanotwinned metals [J]. Nature Materials, 2013, 12(8): 697−702.

[20] CHEN Ming-wei, MA En, HEMKER K J, SHENG Hong-wei, WANG Yin-min, CHENG Xue-mei. Deformation twinning in nanocrystalline aluminum [J]. Science, 2003, 300(5623): 1275−1277.

[21] ZHANG Y F, LI Q, XUE S C, DING J, XIE D Y, LI J, NIU T J, WANG H, WANG H Y, WANG J, ZHANG X. Ultra-strong nanotwinned Al−Ni solid solution alloys with significant plasticity [J]. Nanoscale, 2018, 10(46): 22025−22034.

[22] LI Qiang, XUE Si-chuang, WANG Jian, SHAO Shuai, KWONG A H, GIWA A M, FAN Zhe, LIU Yue, QI Zhi-min, DING Jie, WANG Han, GREER J R, WANG Hai-yan, ZHANG Xing-hang. High-strength nanotwinned Al alloys with 9R phase [J]. Advanced Materials, 2018, 30(11): 1704629.

[23] LI Rui-di, WANG Min-bo, LI Zhi-ming, CAO Peng, YUAN Tie-chui, ZHU Hong-bin. Developing a high-strength Al−Mg−Si−Sc−Zr alloy for selective laser melting: Crack-inhibiting and multiple strengthening mechanisms [J]. Acta Materialia, 2020, 193: 83−98.

[24] GENG Yao-xiang, ZAI Chun-feng, YU Jiang, TANG Hao, LV Hong-wei, ZHANG Zhi-jie. Strength and plasticity improvement induced by strong grain refinement after Zr alloying in the selective laser-melted $AlSiMg_{1.4}$ alloy [J]. Transactions of Nonferrous Metals Society of China, 2024, 34: 2733−2742.

[25] LI Yan-jun, MUGGERUD A M F, OLSEN A, FURU T. Precipitation of partially coherent α-Al(Mn,Fe)Si dispersoids and their strengthening effect in AA 3003 alloy [J]. Acta Materialia, 2012, 60(3): 1004−1014.

[26] WANG Min-bo, LI Rui-di, YUAN Tie-chui, KANG Jing-tao, NIU Peng-da, ZHENG Dan, FAN Zhi-qi. The evolution of quasicrystal during additive manufacturing and aging treatment of a Si-modified Al−Mn−Sc alloy [J]. Materials Science and Engineering: A, 2022, 859: 144206.

[27] SPIERINGS A B, DAWSON K, HEELING T, UGGOWITZER P J, SCHÄUBLIN R, PALM F, WEGENER K. Microstructural features of Sc- and Zr-modified Al−Mg alloys processed by selective laser melting [J]. Materials & Design, 2017, 115: 52−63.

[28] SHEN Jiao-jiao, CHEN Biao, WAN Jie, SHEN Jiang-hua, LI Jin-shan. Effect of annealing on microstructure and mechanical properties of an Al−Mg−Sc−Zr alloy [J]. Materials Science and Engineering: A, 2022, 838: 142821.

[29] DAI Dong-hua, GU Dong-dong. Tailoring surface quality through mass and momentum transfer modeling using a volume of fluid method in selective laser melting of TiC/AlSi10Mg powder [J]. International Journal of Machine Tools and Manufacture, 2015, 88: 95−107.

[30] GONG Hai-jun, RAFI K, GU Heng-feng, STARR T, STUCKER B. Analysis of defect generation in Ti−6Al−4V parts made using powder bed fusion additive manufacturing processes [J]. Additive Manufacturing, 2014, 1: 87−98.

[31] LY S S, RUBENCHIK A M, KHAIRALLAH S A, GUSS G, MATTHEWS M J. Metal vapor micro-jet controls material redistribution in laser powder bed fusion additive manufacturing [J]. Scientific Reports, 2017, 7: 4085.

[32] WANG Lin-zhi, WANG Sen, WU Jiao-jiao. Experimental investigation on densification behavior and surface roughness of AlSi10Mg powders produced by selective laser melting [J]. Optics & Laser Technology, 2017, 96: 88−96.

[33] DU Lei, KE Lin-da, XIAO Mei-li, DOU En-hui, LUO Zhi-qiang, CHEN Yi, LAI Cai-fang. Densification, microstructure and properties of Sc and Zr modified Al−Mn alloy prepared by selective laser melting [J]. Optics Laser Technology, 2022, 148: 107703.

[34] MASKERY I, ABOULKHAIR N T, CORFIELD M R, TUCK C, CLARE A T, LEACH R K, WILDMAN R D, ASHCROFT I A, HAGUE R J M. Quantification and characterisation of porosity in selectively laser melted Al−Si10−Mg using X-ray computed tomography [J]. Materials Characterization, 2016, 111: 193−204.

[35] GENG Yao-xiang, JIA Chao-gang, XU Jun-hua, ZHANG Zhi-jie, JU Hong-bo, WANG Dong-peng, YU Li-hua. Selective laser melting of a novel high-strength Er- and

Zr-modified Al−Mn−Mg alloy [J]. Materials Letters, 2022, 313: 131762.

[36] YU Jiang, GENG Yao-xiang, ZHANG Zhi-jie, JU Hong-bo. Densification, microstructural, and mechanical properties of Al−Mn−Mg−Er−Zr alloy fabricated by laser powder bed fusion [J]. Metals and Materials International, 2023, 29(11): 3235−3248.

[37] LI Yan-jun, ARNBERG L. Quantitative study on the precipitation behavior of dispersoids in DC-cast AA3003 alloy during heating and homogenization [J]. Acta Materialia, 2003, 51(12): 3415−3428.

[38] PAN Shi-wei, QIAN Feng, LI Chu-nan, WANG Zi-dong, LI Yan-jun. Synergistic strengthening by nano-sized α-Al(Mn,Fe)Si and Al_3Zr dispersoids in a heat-resistant Al−Mn−Fe−Si−Zr alloy [J]. Materials Science and Engineering: A, 2021, 819: 141460.

[39] KENDIG K L, MIRACLE D B. Strengthening mechanisms of an Al−Mg−Sc−Zr alloy [J]. Acta Materialia, 2002, 50(16): 4165−4175.

[40] ZHANG Han, GU Dong-dong, DAI Dong-hua, MA Cheng-long, LI Yu-xin, PENG Ruo-lin, LI Shu-hui, LIU Gang, YANG Bi-qi. Influence of scanning strategy and parameter on microstructural feature, residual stress and performance of Sc and Zr modified Al−Mg alloy produced by selective laser melting [J]. Materials Science and Engineering: A, 2020, 788: 139593.

[41] REN Yao-jia, HAN Bo, WU Hong, WANG Jian-chuan, LIU Bin, WEI Bing-qiang, JIAO Zheng-bao, BAKER I. Copper segregation-mediated formation of nanotwins and 9R phase in titanium alloys produced by laser powder bed fusion [J]. Scripta Materialia, 2023, 224: 115115.

[42] RICHTER N A, ZHANG Yi-fan, XIE Dong-yue, SU Rui-zhe, LI Qiang, XUE Si-chuang, NIU Tong-jun, WANG Jian, WANG Hai-yan, ZHANG Xing-hang. Microstructural evolution of nanotwinned Al−Zr alloy with significant 9R phase [J]. Materials Research Letters, 2021, 9(2): 91−98.

[43] WANG Zhi-peng, FANG Qi-hong, FAN Tou-wen, CHEN Dong-chu, LIU Bin, LIU Feng, MA Li, TANG Ping-ying. Effects of solute atoms on 9R phase stabilization in high-performance Al alloys: A first-principles study [J]. JOM, 2019, 71(6): 2047−2053.

[44] RICHTER N A, GONG M Y, ZHANG Y F, NIU T J, YANG B, WANG J, WANG H Y, ZHANG X H. Exploring the deformation behavior of nanotwinned Al−Zr alloy via in situ compression [J]. Journal of Applied Physics, 2022, 132(6): 065104.

[45] OPPRECHT M, GARANDET J P, ROUX G, FLAMENT C, SOULIER M. A solution to the hot cracking problem for aluminium alloys manufactured by laser beam melting [J]. Acta Materialia, 2020, 197: 40−53.

[46] HEO Y U, KIM Y K, KIM J S, KIM J K. Phase transformation of Cu precipitates from bcc to fcc in Fe−3Si−2Cu alloy [J]. Acta Materialia, 2013, 61(2): 519−528.

[47] VARVENNE C, LEYSON G P M, GHAZISAEIDI M, CURTIN W A. Solute strengthening in random alloys [J]. Acta Materialia, 2017, 124: 660−683.

[48] WANG Qing, LI Zhen, PANG Shu-jie, LI Xiao-na, DONG Chuang, LIAW P K. Coherent precipitation and strengthening in compositionally complex alloys: A review [J]. Entropy (Basel), 2018, 20(11): E878.

[49] HU J, SHI Y N, SAUVAGE X, SHA G, LU K. Grain boundary stability governs hardening and softening in extremely fine nanograined metals [J]. Science, 2017, 355(6331): 1292−1296.

时效处理同步提升激光选区熔化低 Sc 含量 Al−Mg−Mn−Sc−Zr 合金的强度和塑性

陈永康[1]，耿遥祥[1]，王 肖，单志法[1]，张志杰[1]，鞠洪博[1,2]

1. 江苏科技大学 材料科学与工程学院，镇江 212003；
2. Department of Mechanical Engineering, CEMMPRE-Centre for Mechanical Engineering,
ARISE, CEMMPRE, University of Coimbra, Coimbra 3030-788, Portugal

摘 要：为了改善激光选区熔化(SLM)低 Sc 含量 Al−Mg−Sc−Zr 合金的成形性和力学性能，以 Mn 元素替代部分 Mg 元素，通过密度测量、显微组织表征和拉伸性能测试，系统地研究了 Al−Mg−Mn−Sc−Zr 合金的 SLM 成形性、显微组织和力学性能。结果表明，通过调整 SLM 工艺参数，可以获得致密的样品。合金呈现精细的等轴柱状双峰晶粒结构。熔体在凝固过程中析出的 Al_3Sc 和 α-Al(Mn,Fe)Si 纳米颗粒有效细化了合金的晶粒尺寸，合金的平均晶粒尺寸为 4.63 μm。合金经 350 °C、2 h 时效处理后，Al_3Sc 纳米颗粒的析出和 9R 相的形成使得合金的强度和伸长率同时提升。本研究表明，通过 SLM 技术，结合后期的热处理工艺可诱导铝合金中长周期堆垛有序相的形成，从而克服铝合金中的强度−塑性矛盾。

关键词：激光选区熔化；低 Sc 含量 Al−Mg−Mn−Sc−Zr 合金；9R 相；Al_3Sc 纳米颗粒；强度−塑性矛盾

(Edited by Wei-ping CHEN)